Self-Aligning Nanojunctions for Integrated Single-

2 Molecule Circuits

- 3 Bo Liu¹, Busra Demir^{2,3}, Caglanaz Akin Gultakti^{2,3}, Jonathan D. Marrs⁴, Yichen Gong¹ Ruihao
- 4 Li¹, Ersin Emre Oren^{2,3}, Joshua Hihath^{1,4,5,*}
- 5 1 Biodesign Center for Bioelectronics and Biosensors at Arizona State University, Tempe, AZ
- 6 85287, USA
- 7 2 Bionanodesign Laboratory, Department of Biomedical Engineering, TOBB University of
- 8 Economics and Technology, Ankara, 06560, Türkiye
- 9 3 Department of Materials Science and Nanotechnology Engineering, TOBB University of
- 10 Economics and Technology, Ankara 06560, Türkiye
- 4 Department of Electrical and Computer Engineering, University of California, Davis. Davis,
- 12 CA 95616, USA
- 13 5 School of Electrical, Computer, and Energy Engineering Arizona State University, Tempe, AZ
- 14 85287, USA
- *Corresponding author. Email: jhihath@asu.edu

16 **ABSTRACT**:

- 17 Robust, high-yield integration of nanoscale components such as graphene nanoribbons,
- 18 nanoparticles, or single-molecules with conventional electronic circuits has proven to be
- challenging.¹⁻⁵ This difficulty arises because the contacts to these nanoscale devices must be
- 20 precisely fabricated with angstrom-level resolution to make reliable connections, and at

manufacturing scales this cannot be achieved with even the highest-resolution lithographic tools. Here we introduce an approach that circumvents this issue by precisely creating nanometer-scale gaps between metallic carbon electrodes using a self-aligning, solution-phase process, which allows facile integration with conventional electronic systems with yields approaching 50%. The electrode separation is controlled by covalently binding metallic single-walled carbon nanotube (mCNT) electrodes to individual DNA duplexes to create mCNT-DNA-mCNT nanojunctions where the gap is precisely matched to the DNA length. These junctions are then integrated with top-down lithographic techniques to create single-molecule circuits that have electronic properties dominated by the DNA in the junction, have reproducible conductance values with low dispersion, and are stable and robust enough to be utilized as active, high-specificity electronic biosensors for dynamic single-molecule detection of specific oligonucleotides, such as those related to the SARS-CoV-2 genome. This scalable approach for high-yield integration of nanometer-scale devices will enable opportunities for manufacturing hybrid electronic systems for a wide range of applications.

KEYWORDS:

- 35 Single-Molecule Electronics, Molecular Devices, Biosensors, Carbon Nanotubes,
- 36 Nanoelectronics, Nanojunction, Self-Alignment

1.INTRODUCTION

The development of self-aligning transistors, where the gate electrode is used as a mask layer to pattern the source and drain, was a key breakthrough that greatly improved the manufacturing yield of semiconductor devices and enabled the continued scaling of electronic systems over many device generations.^{9,10} Now, in recent decades a variety of low-dimensional materials have been

developed with intriguing electronic properties, including CNTs, 11,12 semiconductor nanowires, 13 graphene and other 2D materials, 14,15 and molecular electronic components. 16 However, despite the promise of these systems, the ability to manufacture these devices at-scale for useful applications, and to integrate them into larger-scale lithography processes has remained challenging. 17,18 This issue becomes increasingly prominent as the size-scale decreases to nanometer and molecular levels.^{4,7} For example, while an incredible variety of impressive, molecularly-enabled electronic functions have been demonstrated including quantum interference, 8,19 neuromorphic and memristive activity, 20-22 and optoelectronic control, 23 the utility of these devices has been restricted to understanding physical and chemical processes at the nanoscale due to the difficulties with larger-scale integration.^{2,24,25} To realize the full utility of these systems they must be incorporated into stable, robust, and reliable electronic systems. Thus, inspired by the techniques used for creating self-aligned transistors, we present a method for combining controlled, bottom-up self-assembly processes, with top-down lithographic techniques to create self-aligning single-molecule devices, where the molecule itself is used to define the gap between metallic electrodes, with an overall yield of 44.6% (Fig. 1). We demonstrate the utility of this approach by creating a dynamic, high signal-to-noise ratio (SNR), single-molecule electronic biosensor capable of identifying specific oligonucleotide sequences with high fidelity. This approach provides a basis for developing reliable methods for integrating single-molecule circuits with conventional electronic systems to allow the distinctive functionality of molecular systems to be harnessed at scale.

43

44

45

46

47

48

49

50

51

52

53

54

55

56

57

58

59

60

61

62

63

64

65

To create robust single-molecule junctions we use metallic carbon nanotubes (mCNTs) as nanoelectrodes, which are covalently linked to a molecular bridge in solution phase to create hybrid mCNT-molecule-mCNT junctions. This solution-phase chemical approach ensures that the

gap between the mCNTs is atomically matched with the length of the molecule, this "self-aligning" chemical assembly process circumvents the difficulty of fabricating sub-nanometer precision single-molecule gaps using standard lithography processes. 1,3,5 Instead, these mCNT-molecule-mCNTs can be integrated with conventionally nanofabricated Au electrodes with 300 nm gaps. This combination of bottom-up and top-down processing allows facile integration of single-molecule devices with conventional lithographic processes. Thus, by harnessing the inherent strengths of chemical control of molecular systems, this solution-phase approach allows straightforward junction self-alignment. To create these hybrid junctions, we utilize only metallic CNTs to improve the reproducibility and decrease the dispersion of the conductance properties. DNA is selected as an initial molecular target due to its extensively studied electronic properties, and its potential utility as a biosensing element. 26,27

2.RESULTS AND DISCUSSION

To assemble the mCNT-DNA-mCNT structures we begin with commercially available mCNTs that are soluble in aqueous solutions.²⁸ To protect the mCNT sidewalls during the impending chemical processes, they are wrapped with single-stranded (GT)₂₀ DNA (Figure. 1a,b), which binds strongly to the mCNTs through noncovalent interactions and ensures the continued solubility of the mCNTs in aqueous phases.^{29–32} After this step (see Methods), the DNA wrapped-mCNTs are added to a solution of the target DNA duplexes that are terminated on both ends with an amine group (-(CH₂)₆-NH₂). Then, an amidation reaction between the terminal amines and the exposed carboxylic acid groups on the ends of the mCNTs is initiated using hexafluorophosphate azabenzotriazole tetramethyl uronium (HATU) to create the final, self-aligned, nanojunction in solution that can be subsequently placed on Au electrodes (Figure. 1a).^{33,34}

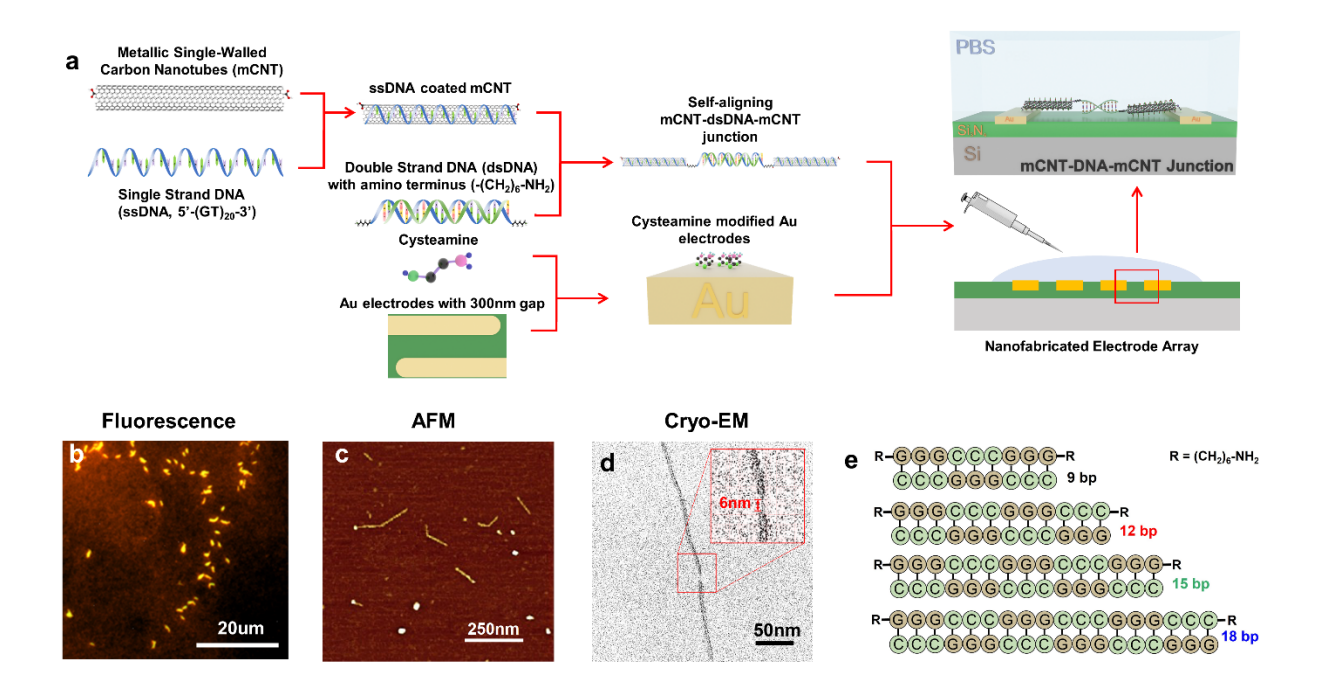


Figure. 1. Development of mCNT-DNA-mCNT junctions. a) Reaction scheme for assembling the self-aligning mCNT-DNA-mCNT junctions and integrating them into the electronic circuit. Carboxyl-terminated mCNT are first wrapped with $(GT)_{20}$, then coupled to amino-functionalized DNA oligonucleotides in PBS buffer to form a self-aligning hybrid structure. Thereafter nanojunctions are drop-cast onto nanofabricated devices where cysteamine modified gold electrodes can anchor the nanojunction with an amide bond to create a robust single molecule junction. b) Fluorescence micrograph of mCNT-DNA-mCNT structures. c) Atomic force microscope image of mCNT-DNA-mCNT structures on a mica surface. d) Cryo-EM micrograph of a mCNT-DNA-mCNT junction with a \sim 6 nm gap structure. e) Series of alternating G:C triplet DNA sequences studied.

To examine the morphological properties of these potential mCNT-DNA-mCNT structures we first utilize fluorescence microscopy. By incubating the samples with ethidium bromide (EtBr) and comparing the resulting fluorescence images (Figure. 1b) with control experiments (Figure. S1), we find that the combination of single-stranded DNA wrapping and an amidation reaction with double-stranded (ds) DNA results in structures that have either single or multiple bends in the backbone, indicative of a linked structure with differing persistence lengths. 35,36 These results are further corroborated by atomic force microscopy (AFM) images where V-shaped features commonly appear (Figure. 1c). The AFM images reveal that the resulting structures are typically

on the order of 250-350 nm and that there are often locations within the structures that possess a smaller cross-section than the rest of the structures (Figure. S2). However, it is difficult to determine whether these features are due to the presence of single-molecules between two mCNTs or due to defects in the single-stranded DNA wrapping process. Thus, to further investigate this possibility, we utilize cryogenic transmission electron microscopy (cryo-EM) to examine the structures. The cryo-EM images indicate that gaps appear in the mCNT structures (Figure. 1e), which is again indicative of the formation of mCNT-DNA-mCNTs. Taken together these characterization approaches consistently suggest molecularly aligned mCNT-DNA-mCNT structures are formed using the above procedure.

Next, we turn to electrical characterization techniques to demonstrate the single-molecule nature of these devices more conclusively. We start by analyzing the electrical properties of a 12 bp sequence with alternating G:C triplets (5'-GGG CCC GGG CCC-3' + complement) with amine linkers on each end (Figure. 1f). To create robust mechanical contacts to the mCNTs, we incubate the nanofabricated substrate with 300 nm gap, Au electrodes in a cysteamine solution overnight prior to adding the mCNT-DNA-mCNT solution (see Methods section for details). Figure. 2a plots 100 consecutive I-V characteristics obtained from a single, bridged 300 nm gap measured in a 100 mM sodium phosphate buffer solution (PBS) at room temperature. For bias voltages swept over a ±0.5 V range, the I-V curves of this 12 bp device are nearly linear indicating ohmic transport behavior. And, as can be seen by the reproducibility of the I-V characteristics and the time series measurements on these devices (Figure. 2b), the structures and conductance values are very stable over time. To examine the reproducibility of the measured conductance values, we examined 58 pairs of 300 nm gap devices across three different chips, and the data from each of these gaps is plotted in Figure. 2c. There are primarily three different conductance regimes visible in this plot.

The grey region shows gaps that are open circuits, indicating no bridging occurred. The yellow region includes high-conductance values. These electrode pairs are either short-circuited during fabrication or bridged by mCNTs (Figure. S3) or bundled structures. The third, pink region, which spans a conductance range of $1x10^{-4\pm1}$ G₀ (where G₀ is the conductance quantum, G₀ = = 77.48 μ S), displays a series of devices with a narrow conductance distribution at $1.02\times10^{-4}\pm0.17\times10^{-4}$ G₀, which is in close agreement with published values for this sequence obtained using the single-molecule break junction approach.³⁷ Scanning electron microscopy (SEM) images of the devices from this conductance range verify that they are bridged by a single entity (Figure. 2d). Notably, of the 58 electrode pairs measured, 26 devices (45%) have a conductance value within this window.

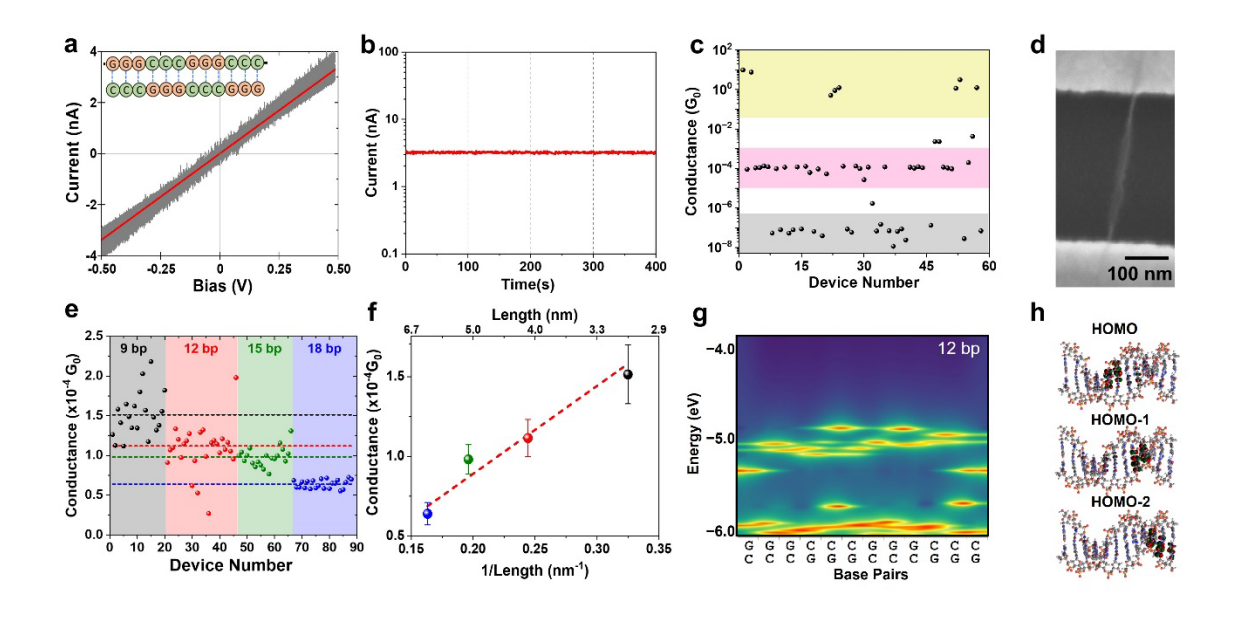


Figure. 2. Charge transport properties of mCNT-DNA-mCNT structures. a) 100 repeated I-V characteristics (gray background) for the 12 bp G:C sequence shown in the inset and a linear fitting to the data (R^2 = 0.989, red line) indicating ohmic transport. b) Current through the device shown in (a) over a 400 s time period. c) Aggregated data from 58 (300 nm) gap devices with the 12 bp sequence. There are 3 distinctive regimes: high conductance (> 10^{-1} G₀, yellow), medium conductance ($1\times10^{-4\pm1}$ G₀, pink), and low conductance (< 10^{-6} G₀, gray). 45% of the devices have a conductance value in the pink region. d) SEM image of one of the devices in the pink region of (c) showing a single bridge between the electrodes. e) Plot of all devices with a conductance in the range of $1\times10^{-4\pm1}$ G₀ for all 4 G:C triplet sequences studied from 9-18 bp, and their average values (dashed lines). f) Conductance of the G:C triplet sequences vs. 1/L. Error bars are standard

deviations calculated from all measurements in plot (e). g) 2D density of states plot for the 12 bp sequence showing a series of delocalized states in a narrow energy range. h) Iso-plots for the 3 highest occupied molecular orbitals (HOMO) demonstrating orbitals are delocalized over several bases.

151

152

153

154

155

156

157

158

159

160

161

162

163

164

165

166

167

168

169

170

171

172

173

174

Upon verifying that the measured conductance values stem from individual bridges between the electrodes, the next step is to demonstrate that these conductance values are determined by single molecules in the mCNT-DNA-mCNT junctions. To do so we take advantage of the selfalignment capabilities of this approach, and systematically measure the conductance of these alternating G:C triplet sequences with lengths of 9, 12, 15, and 18 base pairs. For each molecule, mCNT-DNA-mCNT nanojunctions are first created in solution-phase using the procedure above to ensure that the gap between the mCNTs is perfectly aligned to each molecule's length. After which, the nanojunctions are drop-cast onto their respective chips for electrical characterization. As seen in Fig. 2e the conductance of each of these molecules falls in a narrow region around 1x10⁻¹ ⁴ G₀, which is consistent with previous measurements on GC-rich DNA using Au electrodes. ^{38,39} Moreover, it is also apparent that there is a systematic decrease in the conductance with increasing length (L), and we find that this change in conductance is directly proportional to 1/L (Fig. 2f). This linear dependence of the conductance with length, coupled with the linearity of the I-V traces, are strongly indicative of a hopping-dominated transport mechanism, which has been widely attributed to GC-rich sequences. 40-44 We note that if the DNA was not playing a role in the conductance of these systems, we would not expect any change in the conductance with molecular length because the nominal electrode gap is 300 nm in all cases. Thus, these measurements provide a clear indication that the circuits are derived from single-molecule junctions. Altogether, from the four molecules, we measured 197 electrode pairs and obtained an overall yield of 44.6% (88 bridged gaps).

To further examine hopping as the dominant transport mechanism, we performed molecular dynamics (MD) simulations, density functional theory (DFT) electronic structure calculations, and extracted the density of states for the system. ^{26,45} As can be seen in Fig. 2g,h, for the 12 bp case, the top several occupied molecular orbitals are delocalized over several guanines in the G-triplet regions (see SI Fig. S4 for other molecules). We also find a relatively weak coupling between the triplets (average of 7.5 meV), indicating that a charge would likely traverse these structures by systematically hopping between delocalized energy levels.

Finally, to unambiguously verify the single-molecule nature of these circuits, demonstrate their stability, and examine their utility to serve as active electronic components, we utilize the system as a single-molecule electronic biosensor (Fig. 3). For these experiments, we test whether we can detect the presence of a specific oligonucleotide related to the D614G mutation (aspartic acid swapped for glycine at amino acid residue 614 on the spike protein) in the SARS-CoV-2 virus. The D614G modification was an early mutation that greatly increased the virulence of SARS-CoV-2, 46,47 and by focusing on this coding sequence with a known point mutation difference between the wild type (WT) (GAT codon) and the variant (GGT codon) we can examine the specificity of this detection approach, and its resilience when challenged with potentially interfering targets.

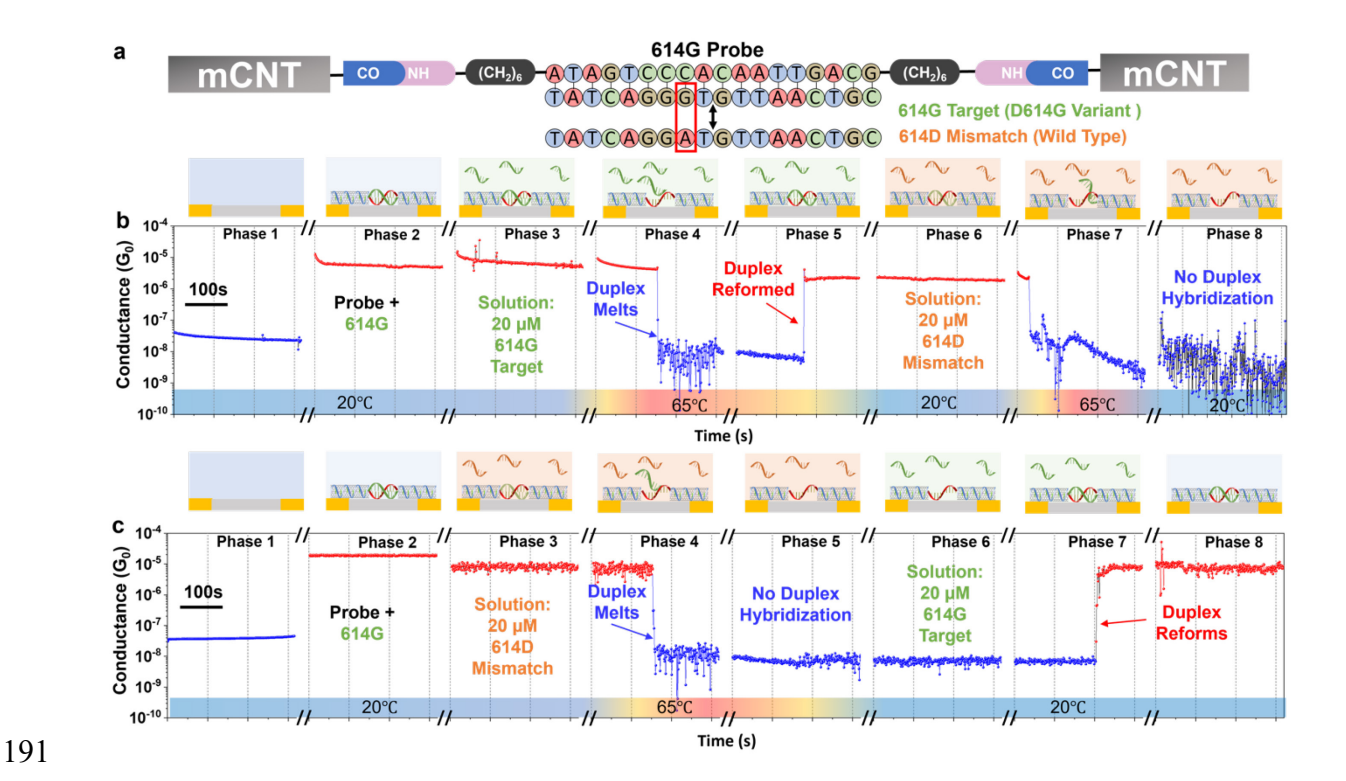


Fig. 3. Electronic oligonucleotide detection using a single-molecule biosensor. a) Schematic representation of the device with the 614G probe and target sequences (614G and 614D). b) Conductance as a function of time for a single mCNT-614G Probe-mCNT junction, with schematics above each phase indicating the process. Phase 1: open-circuit, blank device, prior to junction deposition; Phase 2: Conductance of 614G Probe/Target (PBS, 20°C); Phase 3: Replace solution with 20 µM 614G targets in PBS; Phase 4: Dehybridize the duplex by heating the system at a rate of 0.5°C/s, a conductance drop of 3 orders of magnitude occurs when the solution temperature reaches 65°C indicating DNA dehybridization, with only the single-stranded 614G Probe remaining between the mCNTs resulting in a current below our detectable range; Phase 5: During cooling the junction is reformed when a 614G target from solution binds to the probe sequence to reform a DNA duplex and conductive pathway. Phase 6: Replace solution with the mismatched 614D sequence (WT). Phase 7: Repeat dehybridization process by heating the sample, which again dehybridizes near 65°C. Phase 8: upon cooling no device formation was observed. c) Similar procedure as in b) on a second device, but with sample injection order reversed (first mismatched 614D followed by perfectly matched 614G). Mismatched DNA does not rehybridize in the junction in either case, but the matched 614G sequence does.

192

193

194

195

196

197

198

199

200

201

202

203

204

205

206207

208

209

210

211

For the detection process, we selected an 18 bp DNA sequence identical to the SARS-CoV-2 genome that included several bases on either side of the point mutation D614G, which we refer to as the 614G target sequence (Fig. 3a), and then use a complementary DNA strand with amine linkers on either end as a probe molecule (614G Probe). We then hybridize the probe and target

and subsequently link it to mCNTs as above. This structure is then incubated on a microelectrode chip for 30 minutes before identifying a bridged device. For the device examined, the conductance was stable at $\sim 6 \times 10^{-6}$ G₀ prior to sensing experiments (Fig. 3b, Phase 2). To decrease the possibility of additional mCNT-DNA-mCNT junctions bridging the electrodes during the sensing process, the sample solution is replaced with 20 µM 614G targets in PBS. The conductance remains close to the original value during this solution exchange process (Fig. 3b, Phase 3). Then, to complete the sensor preparation we monitor the conductance of the junction while heating the system at a rate of 0.5°C/s. The conductance suddenly drops to the resolution of the current amplifier when the temperature reaches ~65°C, which corresponds to the calculated melting temperature for this sequence ($T_m = 64.4$ °C). The change in the conductance at this temperature is likely due to the dehybridization of the DNA duplex, and a change in the circuit from transporting through doublestranded DNA to only the single-stranded 614G Probe DNA, which is not conductive due to the lack of π -stacking (Fig. 3b, Phase 4). ^{41,48} Now, with the conductance at effectively zero, we aim to detect the target sequence in the solution. To do so, we decrease the temperature of the cell back toward room temperature, and within several minutes of cooling, there is a sharp increase in the conductance of 3 magnitudes (Fig. 3b, Phase 5), which returned to 2.3×10⁻⁶ G₀ when the DNA probe rehybridizes with a target from the solution. This binary change in the conductance with the formation and breakdown of the device is clear indicator of a single-molecule binding process, ^{49,50} and is commonly used in break-junction based experiments to identify single-molecule conductance values. 51,52 We further note that this change in the conductance is not likely to be due to the breakdown and reformation of the whole device or the contacts, as mCNT junctions are very stable over this temperature range (see Fig. S3).

212

213

214

215

216

217

218

219

220

221

222

223

224

225

226

227

228

229

230

231

232

Next, to gauge the specificity of the system and verify that the binary conductance change occurs due to the molecule instead of changes to the overall bridged structure upon temperature cycling, we repeated this experimental procedure after replacing the 614G solution in the cell with a 20 µM concentration of the wild type, mismatched, 614D sequence in PBS (Fig. 3b, Phase 6). Upon heating, the device again dehybridized at ~65°C, but this time, upon cooling no current increase was observed (Fig. 3b, Phase 6-8). We note that the conductance of the mismatched duplex is $\sim 1 \times 10^{-6}$ G₀ (see Fig. S6), so if the mismatched sequence binds in situ it will be measurable. Thus, this result suggests that the mismatched sequence is not binding to the probe in this configuration. We hypothesize that the lower melting temperature of the mismatched sequence coupled with the potential hindrances introduced by the rigid mCNT gap and the proximity to the surface may inhibit the binding and duplex formation in this constrained configuration on-chip. Nevertheless, this obvious difference in device response between the 614G and 614D targets indicates that the sensing platform can be extremely sensitive to single nucleotide polymorphisms, though additional experiments will be required to determine if this is a general result for mismatched sequences in these devices. However, to confirm this result for sequence, a complementary experiment is performed on a second device, but with the order of target injection reversed (Fig. 3c). In this case the junction conductance still decreases to zero upon heating, and again no conductance increase occurred when cooling with an excess of 614D present in the solution (Fig. 3c, Phase 1-5). However, when the 614D solution is replaced with the perfectly matched 614G sequence (Fig. 3c, Phase 6-8), we again observe junction formation with a conductance of 4.8×10^{-6} G₀. We also note that the entire measurement process takes ~2 hours, demonstrating the long-time stability of these single-molecule junctions. Two additional examples of the 614G Probe/Target binding process are shown in Fig. S7.

234

235

236

237

238

239

240

241

242

243

244

245

246

247

248

249

250

251

252

253

254

255

3.CONCLUSION

257

258

259

260

261

262

263

264

265

266

267

268

269

270

271

272

273

274

275

276

277

278

In conclusion, solution-phase self-alignment of single-molecule electronic devices followed by deposition onto nanofabricated electrodes provides an ability to create dynamic yet stable single-molecule circuits that are easily integrated with conventional lithographic processes. We obtain yields on the order of 50% using only standard, low-resolution photolithography without the addition of low-throughput electron beam or focused ion beam lithography, which enables manufacturing nanoscale electronic circuits based on single-molecule or other nanoscale devices. We show that the resulting DNA-based sensors can reliably detect targeted sequences with very high SNRs and limited possibilities for false positives from interfering or mismatched sequences. This approach offers several potential advantages over conventional viral diagnostic tests. Compared to antigen tests, this approach could quickly pivot to different targets by simply changing the DNA probe sequences as new threats emerge, and it can also obtain strain-level information (i.e. distinguish between alpha and wild-type variants as done here). Typically, to obtain strain-level information it is necessary to do RT-qPCR (Reverse Transcription Quantitative Polymerase Chain Reaction), these assays are expensive, time-consuming, and require highlytrained personnel. This platform also has the potential to be compact and field-deployable. Moreover, this target-agnostic diagnostic platform will allow DNA and RNA sequence detection to be implemented for a wide range of applications in biology, healthcare, and security, for examining the presence of and identifying pathogens, performing liquid biopsies, and tracking disease progression. Moreover, the straightforward chemistry for creating these self-aligning structures provides additional opportunities for integrating other molecular systems with electronic platforms including proteins, catalysts, molecules that undergo field-controllable reactions, as well as more conventional molecular electronic devices such as switches, molecular memory devices, and diodes.

4. METHODS

Preparation of mCNT-DNA-mCNT nanostructures Metallic single wall carbon nanotubes (mCNTs) were purchased from Nano Integris, Inc. Phosphate buffer solution (PBS) and hexafluorophosphate azabenzotriazole tetramethyl uronium (HATU) were purchased from Thermo Fisher Scientific. All other analytical-grade chemicals were purchased from Sigma Aldrich. All DNAs were obtained from Alpha DNA, sequences are listed in the SI.

The mCNT wrapping process is driven primarily by favorable interactions between the ssDNA bases and the mCNT due to van der Waals and hydrophobic interactions. 0.1 mL of the mCNT (1 mg/mL, with Sodium Dodecyl Sulfate(SDS) and Sodium lauryl ether sulfate (SLES)) surfactants) solution is first diluted with 2.5 mL PBS, then 2.5 mL of 5 μM (GT)₂₀ is added. After overnight incubation at room temperature, the mixture is placed in a clean tube surrounded by ice for at least 2 hours under sonication (at the power level of 3W) which is then centrifuged at 5000 rpm (Eppendorf 5415C) for 2 hours to remove insoluble material. The supernatant is collected and diluted with DI water (MilliQ), the volume of (GT)₂₀-dispersed mCNT solutions was kept to 2mL.

To covalently attach DNA duplexes to $(GT)_{20}$ wrapped mCNTs we begin with aminoterminated DNA prepared at a concentration of 5 μ M in 2mL of PBS buffer and mix it with 2 mL $(GT)_{20}$ wrapped mCNTs and ~0.13 mM of Hexafluorophosphate Azabenzotriazole Tetramethyl Uronium (HATU, coupling agent). The mixture was left to react at room temperature for 3 hours under weak sonication. Subsequently, any insoluble material is removed via 15 mins centrifugation at 12000 rpm. The mCNT-DNA-mCNT hybrids are then extracted from the supernatant and readied for transferring onto nanofabricated Au electrodes with 300 nm gaps. *Single-molecule device fabrication* The microelectrode platform used for electrical tests of the nanostructures was fabricated using standard optical lithography techniques. In brief, a Si/Si₃N₄ wafer is first spincoated with hexamethyldisilazane (HMDS) as an adhesive layer, followed by PID controlled

baking at 110°C for 1 min. Then microelectrodes are patterned on the wafer using photolithography with KL5302 Hi-Res Photoresist (Kem Lab). After ~15 s development in CD-26 (TMAH), the wafer is gently rinsed with DI water and blow-dried with nitrogen to stop the development process. Then, a PETS-RIE plasma etcher is employed to etch ~65 nm trenches into the silicon nitride. A Cr(adhesive)/Au multilayer of thickness 10 nm/55 nm is deposited by an e-beam evaporator. The sample is then immersed in MICROPOSITTM Remover 1165 for 90 minutes, and ultrasonicated to lift off residual resist and metal. After that, a 100 nm thick Si₃N₄ insulating layer is deposited using plasma-enhanced chemical vapor deposition (PECVD), to cover the gold electrodes. Micron-sized windows for the probing and sensor areas are patterned using the same photolithography process used previously for the microelectrodes. Finally, a ~100 nm etch into the PECVD Si₃N₄-cover layer is performed using the Plasma-Therma RIE to open the windows and expose the gold electrodes in the desired areas.

To couple the mCNT-DNA-mCNT structures to the Au electrode surfaces we began by immersing the freshly made substrates in a 10 mM solution of cysteamine overnight after 5 mins of UV-ozone treatment. The substrates were then removed from the solution, gently rinsed with DI water, and dried with a stream of nitrogen gas. After device characterization (blank test), a silicone ring was mounted and sealed to sensor area as sample reservoir. Thereafter, the modified Au electrodes were reacted with the mCNT-DNA-mCNT nanostructures through the same amidation reaction in 100 mM PBS solution to covalently bridge the gaps and create a mechanically robust device.

Characterization All the electrical device characterization is performed using a Cascade Micromanipulator probe station equipped with the semiconducting parameter analyzer (Keithley 4200-SCS) at room temperature with a consistent moisture content (30%). For thermal cycling measurements, a PID-controlled heater stage (±0.01 °C) was employed to adjust the temperature (20°C-65°C) at a constant rate. Sample surface temperatures were monitored via an infrared thermometer (Fluke-561). Current sampling measurements were conducted with 0.5 V bias, and at least 3 minutes of monitoring for each electrode. Voltammetry scans (-0.5 V~0.5 V) were conducted subsequently. To ensure that any unattached or nonspecifically bound molecules are completely removed during the sample exchange, we pipette out the spent solution and then rinse the sample reservoir with PBS buffer before introducing a new sample.

Fluorescence: The fluorescence studies of the mCNT-DNA-mCNTs structures with an ethidium bromide (EtBr) intercalating agent were performed with a ZEISS Axio Imager Widefield Fluorescence Microscope. The stock solution of EtBr- nanohybrids is prepared in PBS buffer (containing 1 µM mCNT-DNA-mCNTs and at pH 7.2) and incubated for 30 min at 25 °C before being dropped on a microscope slide for imaging. AFM: The sample solution is deposited onto a piece of mica. Then mica is baked at 60°C under vacuum for 30 mins and rinsed with water to desalt the mica surface. Tapping mode AFM is used to acquire the images under ambient conditions using a Digital Instruments Multimode AFM. Cryo-EM: Cryogenic electron microscopy (Cryo-EM) measurements are carried out using a ThermoFisher Titan Krios electron microscope (Hillsboro, OR). The samples for cryo-TEM are prepared by plunge freezing. A 3 μL of the sample solution is applied to a graphene oxide coated lacey carbon grid (EMS, Hatfield, PA, USA) and then glow-discharged for 15 s with 15 mA current. A thin vicinal film of the CNT sample is formed by blotting with Whatman no. 1 filter paper for approximately 6 s, and the grid is immediately plunged in liquid ethane held at liquid nitrogen temperature. The grid is then transferred to a microscope. Images are recorded at an accelerating voltage of 300 keV and magnifications ranging from 11,500× to 50,000× using K2 summit DED camera in low-dose imaging mode, with the electron dose not exceeding 60 electrons/Angstrom sq. The magnifications results in final pixel sizes ranging from 1-3 Angstroms, and the typical value of the sample under focus ranged from 1-3 microns.

336

337

338

339

340

341

342

343

344

345

346

347

348

349

350

351

352

353

354

355

356

357

358

359

360

361

362

363

364

365

Molecular Dynamics Simulations 9, 12, 15, 18 base pair long DNA molecules are generated using AMBER Nucleic Acid Builder. All structures are neutralized with Na⁺ counterions and added into an octahedral water box which had a 15 Å cutoff from the DNA molecules.

First, water molecules and counterions are subjected to 500 steps of energy minimization, while DNA molecules are restrained with 50 kcal/mol force. Then, 5000 steps of energy minimization are applied to the whole system without any restraint on the molecules. Then, the system is heated to 300 K in NVT ensemble within 100 ps while a 50 kcal/mol restraint force is applied to the DNA molecules. Next, the system equilibrated for 100 ps while a 0.5 kcal/mol restraint force is applied only to the DNA. Finally, the entire system is simulated in an NPT ensemble for 100 ns without any restraining force applied via the AMBER 16⁵³ pmemd CUDA module. For all simulations, bsc1⁵⁴ and TIP3P⁵⁵ force fields are used to describe DNA and water

molecules as well as the counterions, respectively. The particle Mesh Ewald⁵⁶ algorithm is used for long-range electrostatic interactions and a cut-off value of 10 Å is used for the van der Waals interactions. The simulations are performed and recorded every 2 fs, resulting in 50,000 conformations in each trajectory. All bonds with the hydrogen atoms are constrained using the SHAKE algorithm.⁵⁷

To evaluate the electronic properties of each structure, we employ a RMSD based clustering algorithm using VMD software,⁵⁸ which categorizes the DNA conformations observed throughout the simulation time. A cutoff value of 1.75 Å RMSD was chosen to cluster the DNA structures. We select the centroid structures from the most populated cluster (top cluster) which have minimum RMSD difference from the rest of the conformations within the top cluster. Subsequently, energy minimization is performed on the selected structures to relax residual strains resulting from thermal fluctuations during molecular dynamics before quantum mechanical calculations.

DFT Calculations To perform DFT calculations, water molecules and counterions are removed from the previously energy-minimized representative structures. The total charge of each system is set to -16, -22, -28 and -34 for 9, 12, 15 and 18 bp long DNA molecules, respectively. Then, the calculations are carried out using the Gaussian 16⁵⁹ software package with the B3LYP exchange-correlation function and 6-31G(d,p) basis set which provides a balance between memory requirements, computational time and accuracy.^{60,61} Previous studies have demonstrated that the electronic structure of biomolecules in vacuum exhibits a vanishing HOMO-LUMO gap.⁶² As a result, the utilization of implicit or explicit solvation models is necessary. In this work, we assumed that the only effect of the solvent is to modify the equilibrium electronic structure of the DNA molecules, thus we used the implicit solvation method PCM (Polarizable Continuum Model), within the Gaussian 16 software.⁵⁹ Molecular orbitals are generated using the Avogadro software.⁶³

Density of States Calculations

We obtain Fock (H_0) and Overlap (S_0) matrices from DFT calculations and employ a Löwdin transformation 64 to convert H_0 into a Hamiltonian, H, in an orthogonal basis set via the following equation:

$$H = S_0^{(-0.5)} H_0 S_0^{(-0.5)} \tag{1}$$

- The diagonal elements of H matrix account for the energy levels of each atomic orbital, and the
- off-diagonal elements represent the coupling between these atomic orbitals.
- The density of states (DOS) along the molecule in a given energy is calculated using Green's
- function method. First, we compute the retarded Green's function (G^r) as shown in Eq. (2).
- 398 $[E (H + i\eta)]G^r = I$ (2)
- where E is the energy, and H is the Hamiltonian defined in Eq. (1).
- Next, we calculate DOS for each atom (m) by extracting the corresponding diagonal elements
- 401 of the retarded Green's function as follows:

$$DOS(m, E) = \frac{Im(diag(G_m^r(E)))}{\pi}$$
 (3)

- For the 2D DOS plots, we sum up the DOS values of each atom for the corresponding nucleobase
- and energy.
- 405 ASSOCIATED CONTENT
- 406 **Supporting Information**.
- 407 List of DNA Sequences used for experiments.
- 408 Fig. S1. Fluorescent microscopy images of self-aligning mCNT-DNA-mCNT nanohybrids.
- 409 Fig. S2. AFM image of a mCNT-DNA-mCNT nanohybrid.
- 410 Fig. S3. Analysis of Au-mCNT-Au device.
- 411 Fig. S4. Analysis of mCNT-DNA-mCNT devices of different lengths. (9, 15, 18 bp duplexes).
- 412 Fig. S5. 2-dimensional DOS plots and corresponding iso-plots for alternating G:C triplets
- 413 Fig. S6. Conductance vs. Time plot of 614G probe hybridized to 614D Target.
- 414 Fig. S7. Conductance vs. Time plot of 614G probe hybridized to 614G Target.
- The following files are available free of charge.
- 416 **AUTHOR INFORMATION**
- 417 Corresponding Author

418	Corresponding author. Joshua Hihath
419	Email: jhihath@asu.edu
420	Author Contributions
421	Bo Liu, fabricated devices, performed experiments, analyzed results, wrote manuscript.
422	Busra Demir, performed simulations, edited manuscript.
423	Caglanaz Akin Gultakti, performed simulations, edited manuscript.
424	Jonathan Marrs, fabricated devices, edited manuscript.
425	Yichen Gong, performed I-V characterization.
426	Ruihao Li, performed AFM scanning.
427	Ersin Emre Oren, oversaw and analyzed simulations, edited manuscript.
428	Joshua Hihath, conceived experiments, analyzed results, wrote manuscript.
429	
430	ACKNOWLEDGMENTS
431	Authors acknowledge funding support from the National Science Foundation Future
432	Manufacturing Program, NSF-2036865/2328217 and the Keck Foundation. We also thank M.P.
433	Anantram, William Livernois, and Yonggang Ke for fruitful discussions.
434	
435	ASSOCIATED CONTENT
436 437	A preprint of this manuscript is available on the Chemrxiv:
438	B, Liu., B, Demir., C A, Gultakti., J, Marrs., E. E, Oren, & J Hihath.
439 440	Self-Aligning Nanojunctions for Integrated Single-Molecule Circuits. (2023). Chemrxiv 10.26434/chemrxiv-2023-tk0m2 (Jul 06, 2023)

442 **REFERENCES**

- 443 (1) Guo, X.; Small, J. P.; Klare, J. E.; Wang, Y.; Purewal, M. S.; Tam, I. W.; Hong, B. H.; Caldwell,
- 444 R.; Huang, L.; O'brien, S.; Yan, J.; Breslow, R.; Wind, S. J.; Hone, J.; Kim, P.; Nuckolls, C.
- Covalently bridging gaps in single-walled carbon nanotubes with conducting molecules. Science
- 446 (New York, N.Y.) 2006, 311 (5759), 356–359. DOI: 10.1126/science.1120986.
- 447 (2) Roy, S.; Vedala, H.; Roy, A. D.; Kim, D.-H.; Doud, M.; Mathee, K.; Shin, H.; Shimamoto, N.;
- 448 Prasad, V.; Choi, W. Direct electrical measurements on single-molecule genomic DNA using
- single-walled carbon nanotubes. Nano letters 2008, 8 (1), 26–30. DOI: 10.1021/nl0716451.
- 450 Published Online: Dec. 1, 2007.
- 451 (3) Lörtscher, E. Wiring molecules into circuits. Nature nanotechnology 2013, 8 (6), 381–384.
- 452 DOI: 10.1038/nnano.2013.105.
- 453 (4) Puebla-Hellmann, G.; Venkatesan, K.; Mayor, M.; Lörtscher, E. Metallic nanoparticle contacts
- 454 for high-yield, ambient-stable molecular-monolayer devices. Nature 2018, 559 (7713), 232–235.
- 455 DOI: 10.1038/s41586-018-0275-z. Published Online: Jul. 11, 2018.
- 456 (5) Puebla-Hellmann, G.; Venkatesan, K.; Mayor, M.; Lörtscher, E. Metallic nanoparticle contacts
- for high-yield, ambient-stable molecular-monolayer devices. Nature 2018, 559 (7713), 232–235.
- 458 (6) Park, H. j. park, AKL Lim, EH Anderson, AP Aliviastos. Nature 2000, 407, 57.
- 459 (7) Jia, C.; Migliore, A.; Xin, N.; Huang, S.; Wang, J.; Yang, Q.; Wang, S.; Chen, H.; Wang, D.;
- 460 Feng, B. Covalently bonded single-molecule junctions with stable and reversible photoswitched
- 461 conductivity. Science (New York, N.Y.) 2016, 352 (6292), 1443–1445.
- 462 (8) Gehring, P.; Thijssen, J. M.; van der Zant, Herre SJ. Single-molecule quantum-transport
- phenomena in break junctions. Nature Reviews Physics 2019, 1 (6), 381–396.
- 464 (9) Chih-Tang, S. Evolution of the MOS transistor-from conception to VLSI. Proc. IEEE 1988, 76
- 465 (10), 1280–1326. DOI: 10.1109/5.16328.
- 466 (10) Bower, R. W.; Dill, R. G. Insulated gate field effect transistors fabricated using the gate as
- source-drain mask. In 1966 International Electron Devices Meeting; IRE, 1966; pp 102–104. DOI:
- 468 10.1109/IEDM.1966.187724.
- 469 (11) Meyyappan, M. Carbon Nanotube-Based Chemical Sensors. Small (Weinheim an der
- 470 Bergstrasse, Germany) 2016, 12 (16), 2118-2129. DOI: 10.1002/smll.201502555. Published
- 471 Online: Mar. 9, 2016.
- 472 (12) Rao, R.; Pint, C. L.; Islam, A. E.; Weatherup, R. S.; Hofmann, S.; Meshot, E. R.; Wu, F.;
- Zhou, C.; Dee, N.; Amama, P. B.; Carpena-Nuñez, J.; Shi, W.; Plata, D. L.; Penev, E. S.;
- 474 Yakobson, B. I.; Balbuena, P. B.; Bichara, C.; Futaba, D. N.; Noda, S.; Shin, H.; Kim, K. S.;
- Simard, B.; Mirri, F.; Pasquali, M.; Fornasiero, F.; Kauppinen, E. I.; Arnold, M.; Cola, B. A.;

- Nikolaev, P.; Arepalli, S.; Cheng, H.-M.; Zakharov, D. N.; Stach, E. A.; Zhang, J.; Wei, F.;
- 477 Terrones, M.; Geohegan, D. B.; Maruyama, B.; Maruyama, S.; Li, Y.; Adams, W. W.; Hart, A. J.
- 478 Carbon Nanotubes and Related Nanomaterials: Critical Advances and Challenges for Synthesis
- toward Mainstream Commercial Applications. ACS nano 2018, 12 (12), 11756–11784. DOI:
- 480 10.1021/acsnano.8b06511. Published Online: Dec. 5, 2018.
- 481 (13) Ren, Y.; Zou, Y.; Liu, Y.; Zhou, X.; Ma, J.; Zhao, D.; Wei, G.; Ai, Y.; Xi, S.; Deng, Y.
- 482 Synthesis of orthogonally assembled 3D cross-stacked metal oxide semiconducting nanowires.
- 483 Nature materials 2020, 19 (2), 203–211. DOI: 10.1038/s41563-019-0542-x. Published Online:
- 484 Dec. 2, 2019.
- 485 (14) Xu, M.; Liang, T.; Shi, M.; Chen, H. Graphene-like two-dimensional materials. Chemical
- 486 reviews 2013, 113 (5), 3766–3798. DOI: 10.1021/cr300263a. Published Online: Jan. 3, 2013.
- 487 (15) Baringhaus, J.; Ruan, M.; Edler, F.; Tejeda, A.; Sicot, M.; Taleb-Ibrahimi, A.; Li, A.-P.; Jiang,
- 488 Z.; Conrad, E. H.; Berger, C.; Tegenkamp, C.; Heer, W. A. de. Exceptional ballistic transport in
- 489 epitaxial graphene nanoribbons. Nature 2014, 506 (7488), 349–354. DOI: 10.1038/nature12952.
- 490 Published Online: Feb. 5, 2014.
- 491 (16) Xin, N.; Guan, J.; Zhou, C.; Chen, X.; Gu, C.; Li, Y.; Ratner, M. A.; Nitzan, A.; Stoddart, J.
- 492 F.; Guo, X. Concepts in the design and engineering of single-molecule electronic devices. Nature
- 493 Reviews Physics 2019, 1 (3), 211–230.
- 494 (17) Fuller, C. W.; Padayatti, P. S.; Abderrahim, H.; Adamiak, L.; Alagar, N.;
- 495 Ananthapadmanabhan, N.; Baek, J.; Chinni, S.; Choi, C.; Delaney, K. J.; Dubielzig, R.; Frkanec,
- 496 J.; Garcia, C.; Gardner, C.; Gebhardt, D.; Geiser, T.; Gutierrez, Z.; Hall, D. A.; Hodges, A. P.;
- Hou, G.; Jain, S.; Jones, T.; Lobaton, R.; Majzik, Z.; Marte, A.; Mohan, P.; Mola, P.; Mudondo,
- 498 P.; Mullinix, J.; Nguyen, T.; Ollinger, F.; Orr, S.; Ouyang, Y.; Pan, P.; Park, N.; Porras, D.; Prabhu,
- 499 K.; Reese, C.; Ruel, T.; Sauerbrey, T.; Sawyer, J. R.; Sinha, P.; Tu, J.; Venkatesh, A. G.;
- VijayKumar, S.; Le Zheng; Jin, S.; Tour, J. M.; Church, G. M.; Mola, P. W.; Merriman, B.
- Molecular electronics sensors on a scalable semiconductor chip: A platform for single-molecule
- 502 measurement of binding kinetics and enzyme activity. Proceedings of the National Academy of
- 503 Sciences of the United States of America 2022, 119 (5). DOI: 10.1073/pnas.2112812119.
- 504 (18) Goswami, S.; Pramanick, R.; Patra, A.; Rath, S. P.; Foltin, M.; Ariando, A.; Thompson, D.;
- Venkatesan, T.; Goswami, S.; Williams, R. S. Decision trees within a molecular memristor. Nature
- 506 2021, 597 (7874), 51–56. DOI: 10.1038/s41586-021-03748-0. Published Online: Sep. 1, 2021.
- 507 (19) Gunasekaran, S.; Greenwald, J. E.; Venkataraman, L. Visualizing Quantum Interference in
- Molecular Junctions. Nano letters 2020, 20 (4), 2843–2848. DOI: 10.1021/acs.nanolett.0c00605.
- 509 Published Online: Mar. 16, 2020.
- 510 (20) Li, H. B.; Tebikachew, B. E.; Wiberg, C.; Moth-Poulsen, K.; Hihath, J. A memristive element
- based on an electrically controlled single-molecule reaction. Angewandte Chemie 2020, 132 (28),
- 512 11738–11743.
- 513 (21) Goswami, S.; Rath, S. P.; Thompson, D.; Hedström, S.; Annamalai, M.; Pramanick, R.; Ilic,
- B. R.; Sarkar, S.; Hooda, S.; Nijhuis, C. A.; Martin, J.; Williams, R. S.; Goswami, S.; Venkatesan,
- T. Charge disproportionate molecular redox for discrete memristive and memcapacitive switching.

- Nature nanotechnology 2020, 15 (5), 380–389. DOI: 10.1038/s41565-020-0653-1. Published
- 517 Online: Mar. 23, 2020.
- 518 (22) Wang, Y.; Zhang, Q.; Astier, H. P. A. G.; Nickle, C.; Soni, S.; Alami, F. A.; Borrini, A.;
- 519 Zhang, Z.; Honnigfort, C.; Braunschweig, B.; Leoncini, A.; Qi, D.-C.; Han, Y.; Del Barco, E.;
- 520 Thompson, D.; Nijhuis, C. A. Dynamic molecular switches with hysteretic negative differential
- 521 conductance emulating synaptic behaviour. Nature materials 2022, 21 (12), 1403–1411. DOI:
- 522 10.1038/s41563-022-01402-2. Published Online: Nov. 21, 2022.
- 523 (23) Meng, L.; Xin, N.; Hu, C.; Wang, J.; Gui, B.; Shi, J.; Wang, C.; Shen, C.; Zhang, G.; Guo,
- H.; Meng, S.; Guo, X. Side-group chemical gating via reversible optical and electric control in a
- single molecule transistor. Nature communications 2019, 10 (1), 1450. DOI: 10.1038/s41467-019-
- 526 09120-1. Published Online: Mar. 29, 2019.
- 527 (24) Wang, H.; Muren, N. B.; Ordinario, D.; Gorodetsky, A. A.; Barton, J. K.; Nuckolls, C.
- 528 Transducing methyltransferase activity into electrical signals in a carbon nanotube-DNA device.
- 529 Chemical science 2012, 3 (1), 62–65. DOI: 10.1039/C1SC00772F. Published Online: Oct. 20,
- 530 2011.
- 531 (25) Sun, W.; Shen, J.; Zhao, Z.; Arellano, N.; Rettner, C.; Tang, J.; Cao, T.; Zhou, Z.; Ta, T.;
- 532 Streit, J. K.; Fagan, J. A.; Schaus, T.; Zheng, M.; Han, S.-J.; Shih, W. M.; Maune, H. T.; Yin, P.
- Precise pitch-scaling of carbon nanotube arrays within three-dimensional DNA nanotrenches.
- 534 Science (New York, N.Y.) 2020, 368 (6493), 874–877. DOI: 10.1126/science.aaz7440.
- 535 (26) Li, Y.; Artés, J. M.; Demir, B.; Gokce, S.; Mohammad, H. M.; Alangari, M.; Anantram, M.
- P.; Oren, E. E.; Hihath, J. Detection and identification of genetic material via single-molecule
- 537 conductance. Nature nanotechnology 2018, 13 (12), 1167–1173. DOI: 10.1038/s41565-018-0285-
- 538 x. Published Online: Nov. 5, 2018.
- 539 (27) Tsutsui, M.; Matsubara, K.; Ohshiro, T.; Furuhashi, M.; Taniguchi, M.; Kawai, T. Electrical
- detection of single methylcytosines in a DNA oligomer. Journal of the American Chemical Society
- 541 2011, 133 (23), 9124–9128. DOI: 10.1021/ja203839e. Published Online: May. 24, 2011.
- 542 (28) Arnold, M. S.; Green, A. A.; Hulvat, J. F.; Stupp, S. I.; Hersam, M. C. Sorting carbon
- nanotubes by electronic structure using density differentiation. Nature nanotechnology 2006, 1 (1),
- 544 60–65. DOI: 10.1038/nnano.2006.52.
- 545 (29) Hirayama, K.; Kitamura, M.; Lin, N. S.; Nguyen, M. H.; Le, B. D.; Mai, A. T.; Mayama, S.;
- 546 Umemura, K. Attachment of DNA-Wrapped Single-Walled Carbon Nanotubes (SWNTs) for a
- 547 Micron-Sized Biosensor. ACS omega 2022, 7 (50), 47148–47155. DOI:
- 548 10.1021/acsomega.2c06278. Published Online: Dec. 9, 2022.
- 549 (30) Attanzio, A.; Sapelkin, A.; Gesuele, F.; van der Zande, A.; Gillin, W. P.; Zheng, M.; Palma,
- 550 M. Carbon Nanotube-Quantum Dot Nanohybrids: Coupling with Single-Particle Control in
- Aqueous Solution. Small (Weinheim an der Bergstrasse, Germany) 2017, 13 (16). DOI:
- 552 10.1002/smll.201603042. Published Online: Feb. 10, 2017.

- 553 (31) Zheng, M.; Jagota, A.; Semke, E. D.; Diner, B. A.; McLean, R. S.; Lustig, S. R.; Richardson,
- R. E.; Tassi, N. G. DNA-assisted dispersion and separation of carbon nanotubes. Nature materials
- 555 2003, 2 (5), 338–342. DOI: 10.1038/nmat877.
- 556 (32) Zheng, M. Sorting carbon nanotubes. Single-Walled Carbon Nanotubes: Preparation,
- Properties and Applications 2019, 129–164.
- 558 (33) Hunter, James H., et al. "Highly efficient on-DNA amide couplings promoted by micelle
- forming surfactants for the synthesis of DNA encoded libraries." Chemical Science 12.27 (2021):
- 560 9475-9484.
- 561 (34) Palma, M.; Wang, W.; Penzo, E.; Brathwaite, J.; Zheng, M.; Hone, J.; Nuckolls, C.; Wind, S.
- J. Controlled formation of carbon nanotube junctions via linker-induced assembly in aqueous
- solution. Journal of the American Chemical Society 2013, 135 (23), 8440-8443. DOI:
- 564 10.1021/ja4018072. Published Online: May. 29, 2013.
- 565 (35) Oruc, B.; Celik, S.; Hayat Soytas, S.; Unal, H. DNA Directed Self-Assembly of Single Walled
- 566 Carbon Nanotubes into Three-Way Junction Nanostructures. ACS omega 2018, 3 (4), 4157–4162.
- DOI: 10.1021/acsomega.8b00306. Published Online: Apr. 12, 2018.
- 568 (36) Freeley, M.; Worthy, H. L.; Ahmed, R.; Bowen, B.; Watkins, D.; Macdonald, J. E.; Zheng,
- M.; Jones, D. D.; Palma, M. Site-Specific One-to-One Click Coupling of Single Proteins to
- 570 Individual Carbon Nanotubes: A Single-Molecule Approach. Journal of the American Chemical
- 571 Society 2017, 139 (49), 17834–17840. DOI: 10.1021/jacs.7b07362. Published Online: Nov. 29,
- 572 2017.
- 573 (37) Alangari, M.; Demir, B.; Gultakti, C. A.; Oren, E. E.; Hihath, J. Mapping DNA Conformations
- 574 Using Single-Molecule Conductance Measurements. Biomolecules 2023, 13 (1). DOI:
- 575 10.3390/biom13010129. Published Online: Jan. 8, 2023.
- 576 (38) Artés, J. M.; Li, Y.; Qi, J.; Anantram, M. P.; Hihath, J. Conformational gating of DNA
- 577 conductance. Nature communications 2015, 6, 8870. DOI: 10.1038/ncomms9870. Published
- 578 Online: Dec. 9, 2015.
- 579 (39) Xiang, L.; Palma, J. L.; Bruot, C.; Mujica, V.; Ratner, M. A.; Tao, N. Intermediate tunnelling-
- hopping regime in DNA charge transport. Nature chemistry 2015, 7 (3), 221–226. DOI:
- 581 10.1038/nchem.2183.
- 582 (40) Xu, B., Zhang, Li, X., & Tao. (2004). Direct conductance measurement of single DNA
- molecules in aqueous solution. Nano letters, 4(6), 1105-1108.
- 584 (41) Artés, J. M., Li, Y., Qi, J., Anantram, M. P., & Hihath, J. (2015). Conformational gating of
- 585 DNA conductance. Nature communications, 6(1), 8870.
- 586 (42) Li, Yuanhui, Juan M. Artés, and Joshua Hihath. "Molecular Electronics: Long Range
- 587 Charge Transport in Adenine Stacked RNA: DNA Hybrids (Small 4/2016)." Small 12.4 (2016):
- 588 409-409.
- 589 (43) Lewis, F. D.; Liu, X.; Liu, J.; Miller, S. E.; Hayes, R. T.; Wasielewski, M. R. Direct
- measurement of hole transport dynamics in DNA. Nature 2000, 406 (6791), 51–53.

- 591 (44) Bixon, M.; Jortner, J. Charge transport in DNA via thermally induced hopping. Journal of the
- 592 American Chemical Society 2001, 123 (50), 12556–12567. DOI: 10.1021/ja010018p.
- 593 (45) Qi, J.; Edirisinghe, N.; Rabbani, M. G.; Anantram, M. P. Unified model for conductance
- through DNA with the Landauer-Büttiker formalism. Phys. Rev. B 2013, 87 (8). DOI:
- 595 10.1103/PhysRevB.87.085404.
- 596 (46) Guo, C.; Tsai, S.-J.; Ai, Y.; Li, M.; Anaya, E.; Pekosz, A.; Cox, A.; Gould, S. J. The D614G
- 597 mutation redirects SARS-CoV-2 spike to lysosomes and suppresses deleterious traits of the furin
- 598 cleavage site insertion mutation. Science Advances 2022, 8 (51), eade 5085.
- 599 (47) Zhang, L.; Jackson, C. B.; Mou, H.; Ojha, A.; Peng, H.; Quinlan, B. D.; Rangarajan, E. S.;
- Pan, A.; Vanderheiden, A.; Suthar, M. S.; Li, W.; Izard, T.; Rader, C.; Farzan, M.; Choe, H. SARS-
- 601 CoV-2 spike-protein D614G mutation increases virion spike density and infectivity. Nature
- 602 communications 2020, 11 (1), 6013. DOI: 10.1038/s41467-020-19808-4. Published Online: Nov.
- 603 26, 2020.
- 604 (48) Li, Y., Artés, J. M., Demir, B., Gokce, S., Mohammad, H. M., Alangari, M., ... & Hihath, J.
- 605 (2018). Detection and identification of genetic material via single-molecule conductance. Nature
- 606 nanotechnology, 13(12), 1167-1173.
- 607 (49) Haiss, W.; Wang, C.; Grace, I.; Batsanov, A. S.; Schiffrin, D. J.; Higgins, S. J.; Bryce, M. R.;
- 608 Lambert, C. J.; Nichols, R. J. Precision control of single-molecule electrical junctions. Nature
- 609 materials 2006, 5 (12), 995–1002. DOI: 10.1038/nmat1781. Published Online: Nov. 26, 2006.
- 610 (50) Tang, L.; Yi, L.; Jiang, T.; Ren, R.; Paulose Nadappuram, B.; Zhang, B.; Wu, J.; Liu, X.;
- 611 Lindsay, S.; Edel, J. B. Measuring conductance switching in single proteins using quantum
- tunneling. Science Advances 2022, 8 (20), eabm8149.
- 613 (51) Haiss, W., Nichols, R. J., van Zalinge, H., Higgins, S. J., Bethell, D., & Schiffrin, D. J. (2004).
- Measurement of single molecule conductivity using the spontaneous formation of molecular wires.
- Physical Chemistry Chemical Physics, 6(17), 4330-4337.
- 616 (52) Haiss, W., Wang, C., Grace, I., Batsanov, A. S., Schiffrin, D. J., Higgins, S. J., ... & Nichols,
- R. J. (2006). Precision control of single-molecule electrical junctions. Nature materials, 5(12), 995-
- 618 1002.
- 619 (53) D.A. Case R.M. Betz, D. S. C., T. E. Cheatham, III, T. A. Darden, R. E. Duke, T. J. Giese,
- H. Gohlke, A. W. Goetz, N. Homeyer, S. Izadi, P. Janowski, J. Kaus, A. Kovalenko, T. S. Lee, S.
- 621 LeGrand, P. Li, T. Luchko, R. Luo, B. Madej, K. M. Merz, G. Monard, P., J. T. Berryman.
- 622 AMBER 2016. (2016).
- 623 (54) Ivani, I.; Dans, P. D.; Noy, A.; Pérez, A.; Faustino, I.; Hospital, A.; Walther, J.; Andrio, P.;
- 624 Goñi, R.; Balaceanu, A.; Portella, G.; Battistini, F.; Gelpí, J. L.; González, C.; Vendruscolo, M.;
- Laughton, C. A.; Harris, S. A.; Case, D. A.; Orozco, M. Parmbscl: a refined force field for DNA
- 626 simulations. Nature methods 2016, 13 (1), 55–58. DOI: 10.1038/nmeth.3658. Published Online:
- 627 Nov. 16, 2015.

- 628 (55) Jorgensen, W. L.; Chandrasekhar, J.; Madura, J. D.; Impey, R. W.; Klein, M. L. Comparison
- of simple potential functions for simulating liquid water. The Journal of Chemical Physics 1983,
- 630 79 (2), 926–935. DOI: 10.1063/1.445869.
- 631 (56) Darden, T.; York, D.; Pedersen, L. Particle mesh Ewald: An N ·log(N) method for Ewald
- sums in large systems. The Journal of Chemical Physics 1993, 98 (12), 10089–10092. DOI:
- 633 10.1063/1.464397.
- 634 (57) Miyamoto, S.; Kollman, P. A. Settle: An analytical version of the SHAKE and RATTLE
- algorithm for rigid water models. J. Comput. Chem. 1992, 13 (8), 952–962.
- 636 (58) Humphrey, W.; Dalke, A.; Schulten, K. VMD: visual molecular dynamics. Journal of
- 637 molecular graphics 1996, 14 (1), 33–38.
- 638 (59) Frisch, M. J. et al. Gaussian 16 Revision C.01. 2016. https://gaussian.com/g16/g16src
- 639 (60) Russo, N.; Toscano, M.; Grand, A. Theoretical determination of electron affinity and
- ionization potential of DNA and RNA bases. J. Comput. Chem. 2000, 21 (14), 1243–1250. DOI:
- 641 10.1002/1096-987X(20001115)21:14<1243:AID-JCC3>3.0.CO;2-M.
- 642 (61) Cauët, E.; Dehareng, D.; Liévin, J. Ab initio study of the ionization of the DNA bases:
- ionization potentials and excited states of the cations. The journal of physical chemistry. A 2006,
- 644 110 (29), 9200–9211. DOI: 10.1021/jp0617625.
- 645 (62) Rudberg, E. Difficulties in applying pure Kohn-Sham density functional theory electronic
- structure methods to protein molecules. Journal of physics. Condensed matter: an Institute of
- 647 Physics journal 2012, 24 (7), 72202. DOI: 10.1088/0953-8984/24/7/072202. Published Online:
- 648 Jan. 6, 2012.

- 649 (63) Hanwell, M. D.; Curtis, D. E.; Lonie, D. C.; Vandermeersch, T.; Zurek, E.; Hutchison, G. R.
- Avogadro: an advanced semantic chemical editor, visualization, and analysis platform. Journal of
- 651 cheminformatics 2012, 4 (1), 1–17.
- 652 (64) Jorge L. D'Amato and Horacio M. Pastawski. Conductance of a disordered linear chain
- 653 including inelastic scattering events. Physical Review B, 1990, 41(11)7411–7420.